Research Square

Preprints are preliminary reports that have not undergone peer review.
They should not be considered conclusive, used to inform clinical practice,
or referenced by the media as validated information.

Hydrological impacts of historical and projected land use/land cover change in the Hyrcanian forests, Iran

Faezeh KhorshidSokhangouy
Tarbiat Modares University
Hamidreza Moradi
hrmoradi@modares.ac.ir

Tarbiat Modares University
Arash Malekian
University of Tehran
Vahid Moosavi
Tarbiat Modares University
Prasad Daggupati
University of Guelph

Article

Keywords: Geospatial analysis, Hydrological modelling, Land-use dynamics, Water resources management

Posted Date: November 25th, 2026

DOI: https://doi.org/10.21203/rs.3.rs-11720079/v1

License: This work is licensed under a Creative Commons Attribution 4.0 International License.
Read Full License

Additional Declarations: No competing interests reported.

Hydrological impacts of historical and projected land use/land cover change in the Hyrcanian forests, Iran

Faezeh KhorshidSokhangouy[1], **Hamidreza Moradi**[1]✉, **Arash Malekian**[2], **Vahid Moosavi**[1] & **Prasad Daggupati**[3]

[1]Department of Watershed Management Engineering, Faculty of Natural Resources, Tarbiat Modares University, Noor, Mazandaran, Iran.

[2]Department of Reclamation of Arid and Mountainous Regions, University of Tehran, Karaj, Iran.

[3]School of Engineering, University of Guelph, Guelph, Ontario, Canada.

✉ email: hrmoradi@modares.ac.ir

Land use/land cover (LU/LC) change may alter runoff and streamflow. However, its effect under constant climate remains poorly understood in the Talar Watershed, located in the Hyrcanian forests of Iran. We used the Soil and Water Assessment Tool (SWAT) to compare the hydrological response to three historical LU/LC maps (2001, 2012 and 2023, overall accuracy 91.4–93.0%) and two exploratory scenarios (2034 and 2045) projected with the Land Change Modeler. The model simulated monthly streamflow with satisfactory agreement (NSE 0.59 for calibration and 0.53 for validation). Only the LU/LC map differed between simulations. Between 2001 and 2045, forest and rangeland declined by 17.6% and 25.1%, whereas agricultural, barren and residential land increased. Compared with 2001, all later maps reduced actual evapotranspiration by 8.2–9.2% and percolation by 27.0–32.2%, and increased surface runoff from 8.5 to 44.7–57.9 mm year^{-1}. Mean annual streamflow at the Shirgah outlet rose from 5.40 to 6.36–6.93 m^3 s^{-1} (17.7–28.2%), with the largest increase in 2045 and the smallest in 2023, while groundwater flow and lateral flow decreased by 23.5–27.8% and 11.3–13.6%. Overall, LU/LC change shifted the simulated water balance from subsurface flow toward surface runoff, conditional on the fixed climate and a single calibrated parameter set.

Keywords Geospatial analysis, Hydrological modelling, Land-use dynamics, Water resources management

Introduction

Land use/land cover (LU/LC) change represents a primary driver of hydrological alterations in watersheds. It modifies vegetation cover, soil exposure, surface roughness, and imperviousness. As a result, the partitioning of precipitation into evapotranspiration, infiltration, percolation, surface runoff, groundwater flow and streamflow may be altered [1–3]. Quantifying these effects is therefore necessary for water resource management, flood risk reduction and land-use planning [4,5].

Remote sensing (RS) and geographic information systems (GIS) provide consistent information on past LU/LC change. Based on these records, models can project possible future LU/LC patterns [6–8]. The Land Change Modeler (LCM) in TerrSet estimates the quantity of change with a Markov chain. It models the transition potential of each class from driver variables using a multilayer perceptron (MLP) neural network [7]. A growing body of literature has coupled historical and projected LU/LC maps with hydrological models across several basins. These studies reported changes in surface runoff, evapotranspiration, percolation, groundwater flow, water yield and discharge [2,9,10]. However, the magnitude and direction of these responses vary considerably across basins.

The Talar Watershed is part of the Hyrcanian forest belt along the southern coast of the Caspian Sea. This belt is recognised internationally for its ancient temperate broadleaf forests and high biodiversity [11]. Nevertheless, forest degradation, agricultural expansion, urban sprawl, road construction, grazing and mining have increased pressure on the region [12,13].

Previous studies in the Talar Watershed have examined land-use effects on runoff and nitrate transport [12], landscape change [13], soil erosion and sediment yield [14–16], and climatic and anthropogenic influences on streamflow [17]. However, previous research has rarely evaluated and compared the hydrological effects of historical and projected LU/LC trajectories within a unified modelling framework. In particular, the extent to which these patterns alter evapotranspiration, percolation, surface runoff and streamflow under stationary climate conditions and constant calibrated parameters remains poorly understood. Such a comparison can clarify how forest and rangeland conversion redistributes water among hydrological components, and whether the LU/LC map with the greatest surface runoff also produces the highest outlet streamflow. A common shortcoming in previous modelling efforts is representing agricultural land as a single generic class [18–20], which overlooks critical differences in hydrological responses associated with crop types and management practices. In this study, crop-specific planting, harvesting and irrigation operations were defined in the Soil and Water Assessment Tool (SWAT) management files for the main crop groups of the watershed.

To fill these gaps, the primary objective of this study is to evaluate and compare the hydrological impacts of three historical LU/LC maps (2001, 2012 and 2023) and two exploratory future scenarios (2034 and 2045) using the SWAT model. The projected maps are generated with the LCM. Agricultural land is represented by crop-specific management operations rather than a single generic class. The analysis evaluates changes in water-balance components and mean annual discharge at the watershed outlet. The study addresses three questions. (1) How did past LU/LC change affect surface runoff and the partitioning of water? (2) How could projected LU/LC change affect watershed hydrology in 2034 and 2045? (3) Which LU/LC map produces the largest increase in surface runoff depth (mm), and how is this reflected in mean annual streamflow, expressed as discharge ($m^3\ s^{-1}$), at the outlet?

Methods

Study area

The Talar Watershed is located in northern Iran, on the southern coast of the Caspian Sea and the northern slopes of the Alborz Mountains [13]. It extends from 35°53′40″ to 36°24′40″ N and from 52°30′00″ to 53°21′40″ E. According to the SWAT delineation, it covers about 1,752 km^2, with elevations ranging from 203 to 3,857 m above sea level (Fig. 1). The Talar River drains northward into the Caspian Sea [13]. Precipitation data were obtained from four stations (Gharakheil, Alasht, Pol Sefid, and Shirgah), whereas temperature records were obtained from three synoptic stations. The Shirgah hydrometric station, located near the watershed outlet, provided the streamflow records used for model calibration and validation (Fig. 1). The monitoring records span the period from 23 September 2003 to 22 September 2021. Mean annual precipitation, calculated as the area-weighted average across hydrological response units (HRUs) over the 2006–2020 baseline period is 587.5 mm.

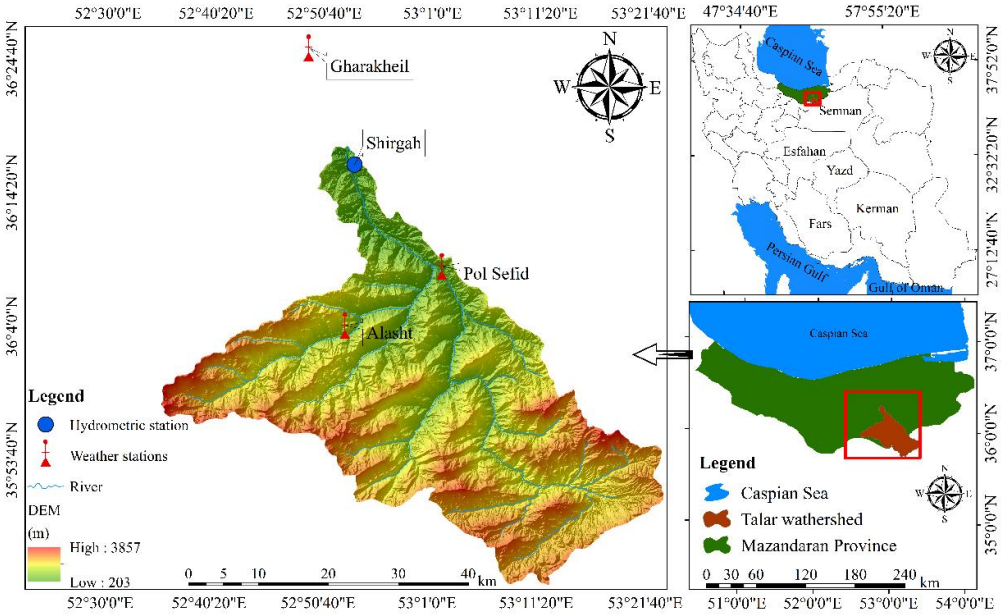


Fig. 1. Geographical location, digital elevation model (DEM), river network and gauging stations of the study area.

Methodological workflow

The overall workflow is illustrated in Fig. 2. Historical LU/LC maps for 2001, 2012 and 2023 were prepared using ENVI software based on Landsat imagery, Google Earth imagery and field observations. These maps were subsequently employed in TerrSet to project the 2034 and 2045 maps via the LCM. The SWAT model was set up using DEM, soil, LU/LC, slope, management and climate data, followed by sensitivity analysis, calibration and validation. Finally, simulations were performed using the calibrated model for each of the five LU/LC maps to quantify outlet streamflow (FLOW_OUT) and water-balance components.

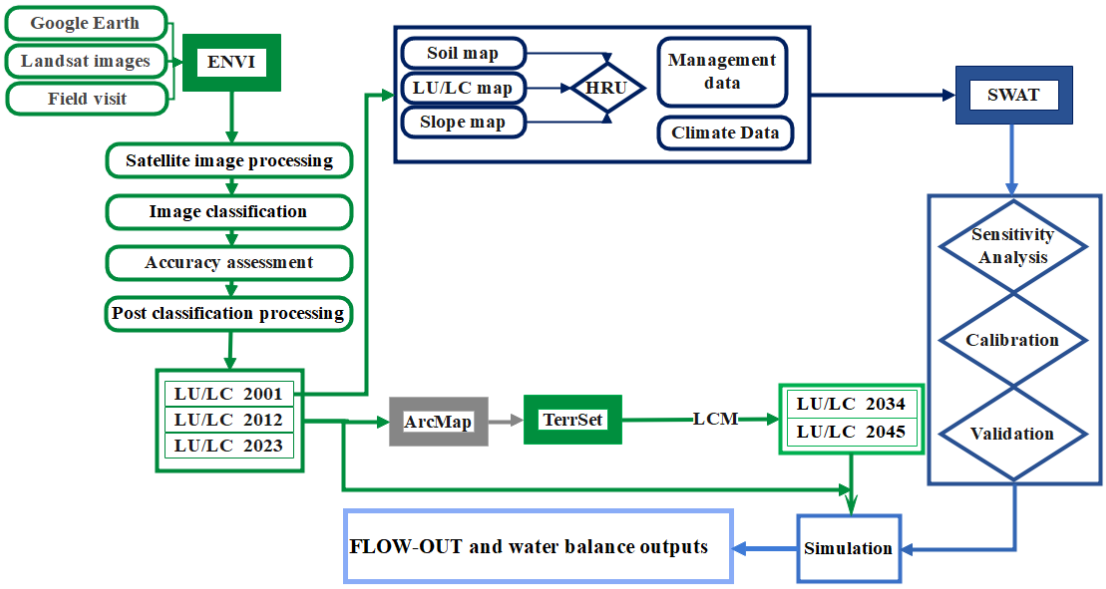


Fig. 2. Methodological workflow for integrating LU/LC classification, LCM prediction, and SWAT-based hydrological simulation in the study.

Dataset

Satellite imagery

Landsat Collection 2 Level-2 surface reflectance images at a 30 m spatial resolution were employed for August 2001 (Landsat 7 ETM+), May 2012 (Landsat 5 TM), and August 2023 (Landsat 9 OLI-2) [21–23]. The 2001 and 2023 scenes were obtained from the United States Geological Survey (USGS), whereas the 2012 scene was retrieved via the Google Earth Engine platform [24]. To minimise atmospheric interference, only scenes with less than 5% cloud cover were selected. USGS Level-2 products are pre-corrected for atmospheric effects. Surface reflectance for Landsat 5 TM and Landsat 7 ETM+ is generated via the Landsat Ecosystem Disturbance Adaptive Processing System (LEDAPS) [25], whereas Landsat 9 data are processed using the Land Surface Reflectance Code (LaSRC) [26]. Therefore, no further atmospheric correction or cloud masking was deemed necessary. Image pre-processing and classification analyses were performed using ENVI software. A total of 4,952 reference samples across five LU/LC classes (forest, rangeland, agricultural land, residential areas, and barren land) were collected using GPS coordinates and Google Earth imagery. Spectral bands were combined with selected spectral indices in order to enhance class separability, and the mean Normalised Difference Vegetation Index (NDVI) layer was derived using Google Earth Engine [24].

Terrain and soil data

A 30 m digital elevation model (DEM) from the Shuttle Radar Topography Mission (SRTM) was downloaded from the USGS EarthExplorer platform [27]. The DEM was employed to delineate the watershed, extract the stream network, and define slope classes and subbasins. The soil map and its associated attributes were retrieved from Mohammadi et al. [28]. The DEM, soil, and LU/LC layers were then incorporated into ArcSWAT as raster datasets.

Climate and streamflow data

Daily precipitation as well as maximum and minimum temperature records from the Alasht, Pol Sefid, and Gharakheil stations were provided by the Iran Meteorological Organization (IRIMO) (Fig. 1). Daily precipitation and streamflow records at the Shirgah hydrometric station were obtained from the Ministry

of Energy of Iran. Snow processes were simulated using the default SWAT snow parameters. The model simulation was performed over the period from 2003 to September 2021, with the initial years (2003–2005) designated as a warm-up period to minimise the effects of initial soil-water and groundwater conditions. Only complete calendar years were included in the analyses; consequently, the effective simulation period spans 2006–2020.

Agricultural management

Agricultural land was classified into five major crop groups, namely alfalfa, rice, wheat, apple orchards, and citrus orchards, in addition to a generic agricultural class, which were selected based on local knowledge of the prevailing cropping patterns. Planting and harvesting dates, as well as irrigation schedules and amounts, were parameterised within the SWAT management files for each crop group using records obtained from the Agricultural Jihad Organization and the database of the Soil and Water Research Institute [29]. Crop proportions within agricultural land were assigned manually as fixed values and applied consistently across all LU/LC maps; consequently, simulated crop areas reflect these predefined proportions and the HRU delineation rather than independently mapped crop distributions. Irrigation amounts were specified in accordance with approximate crop water requirements and local agronomic conditions rather than direct field measurements.

Land use/land cover mapping and accuracy assessment

Seven layers were stacked as inputs for classification: the blue, green, and red bands, the Normalised Difference Built-up Index (NDBI) [30], the NDVI [31], the Modified Normalised Difference Water Index (MNDWI) [32], and the annual mean NDVI. The indices were calculated as follows (Eqs. 1–3):

$$\mathrm{NDBI} = \frac{(\rho_{\mathrm{SWIR1}} - \rho_{\mathrm{NIR}})}{(\rho_{\mathrm{SWIR1}} + \rho_{\mathrm{NIR}})} \quad (1)$$

$$\mathrm{NDVI} = \frac{(\rho_{\mathrm{NIR}} - \rho_{\mathrm{Red}})}{(\rho_{\mathrm{NIR}} + \rho_{\mathrm{Red}})} \quad (2)$$

$$\mathrm{MNDWI} = \frac{(\rho_{\mathrm{Green}} - \rho_{\mathrm{SWIR1}})}{(\rho_{\mathrm{Green}} + \rho_{\mathrm{SWIR1}})} \quad (3)$$

where ρ denotes surface reflectance in the blue, green, red, near-infrared (NIR), and first shortwave-infrared (SWIR1) bands, which correspond to bands 1–5 for Landsat 5 and 7 and bands 2–6 for Landsat 9. The annual mean NDVI was computed in Google Earth Engine by averaging all available Landsat NDVI observations within each year.

The watershed was classified into four classes (agriculture, barren land, rangeland, and forest) in ENVI 5.3 using four supervised algorithms that are widely applied in LU/LC mapping [33]: support vector machine (SVM), maximum likelihood classifier (MLC), minimum distance classifier (MDC), and neural network (NN). These four classes were mapped by supervised classification; residential areas, the fifth class, were added separately (see below). All four algorithms were trained on point samples collected from the watershed and Google Earth imagery. Their accuracy was then assessed with a separate set of 454 validation polygons (agriculture 151, rangeland 135, forest 118, and barren land 50), digitised on Google Earth imagery to ensure no overlap with the training points. The same validation polygons were used for the three years. For each year, the algorithm with the highest overall accuracy and Kappa coefficient was used to produce the final map: SVM for 2001 and MLC for 2012 and 2023. All layers and maps shared the same spatial extent, projection, cell size, and pixel alignment.

Residential areas are small and scattered across the watershed, and mixed pixels at 30 m resolution reduced their classification accuracy. The residential areas for 2023 were therefore delineated manually

in Google Earth and added to the 2023 map. For 2001 and 2012, they were derived using a MATLAB script from this urban layer and the NDVI of each year, and added to the corresponding maps. Accuracy was assessed using confusion matrices, from which the overall accuracy, Kappa coefficient, producer's accuracy, user's accuracy, and F1-score for each class were calculated. The F1-score is the harmonic mean of the producer's and user's accuracies, ranging from 0 to 100%; it summarises omission and commission errors in a single metric.

Future LU/LC projection

Future LU/LC maps were generated using the Land Change Modeler (LCM) in TerrSet 2020 [7]. LCM combines a Markov chain, which estimates the quantity of change between two dates, with a multilayer perceptron (MLP) neural network, which produces transition potential maps from a set of driver variables. The drivers were distance from residential areas, forest, barren land, agricultural land, and rangeland, together with slope, aspect, and an evidence likelihood layer. The evidence likelihood layer was generated in LCM from the change map produced by the change analysis of the calibration period. The set of variables used differed among transitions.

The model was first validated by simulating the 2023 LU/LC map from the changes observed during 2001–2012 and comparing it with the classified 2023 map, which served as the reference, using the VALIDATE module in TerrSet. Agreement was quantified with the Kappa indices $K_{standard}$ (overall agreement relative to chance), K_{no} (agreement relative to a baseline with no information about class quantities or locations), $K_{location}$ (agreement in the spatial allocation of classes), and $K_{locationStrata}$ (location agreement within strata) [7,34].

Because LCM estimates transition probabilities for a time step equal to the period of observed change, the projection horizon was set equal to the length of the calibration period. The 2034 map, 11 years after the 2023 baseline, was therefore projected from the changes observed during 2012–2023, and the 2045 map, 22 years after the baseline, from the changes observed during 2001–2023. The projections assume that the patterns of change observed in each historical period continue unchanged. The projected maps were then used as LU/LC inputs to the calibrated SWAT model to simulate the hydrological response of the watershed under these scenarios.

SWAT model setup

ArcSWAT 2012, integrated with ArcGIS, was used to simulate the hydrological response of the Talar Watershed under historical and projected land use/land cover (LU/LC) maps. SWAT is a semi-distributed, process-based model that represents hydrological processes using information on climate, topography, soils, land cover, and management practices [35–37]. The watershed is divided into subbasins, which are further subdivided into HRUs, each representing a distinct combination of land use, soil type, and slope class.

The DEM was used to delineate the watershed, extract the stream network, and define 21 subbasins. Streams were defined using a contributing-area threshold of 3,503.3 ha (35.0 km^2). Strahler orders were calculated from the upstream–downstream connectivity in the exported ArcSWAT reach table. The resulting 21-reach network has a maximum Strahler order of 3, which is also the order of the outlet reach.

HRUs were generated separately for each LU/LC map using thresholds of 10% for land use, 20% for soil, and 30% for slope, yielding 497, 502, 527, 495, and 497 HRUs for the 2001, 2012, 2023, 2034, and 2045 maps, respectively. The DEM, soil layer, slope classification, and thresholds were identical across maps; the number and composition of HRUs differed only because each LU/LC map was processed separately.

The model was driven by daily weather data, and potential evapotranspiration was estimated using the Penman–Monteith method [37]. Agricultural land was represented by six classes, namely rice (RICE), winter wheat (WWHT), alfalfa (ALFA), apple (APPL), orange (ORAN), and a generic agricultural class (AGRL). Planting, harvesting, and irrigation dates were specified in the management schedules of the relevant agricultural HRUs, and the same management assumptions were applied in all simulations.

Sensitivity analysis, calibration and validation

Parameter sensitivity analysis, calibration, validation, and uncertainty assessment were carried out with the Sequential Uncertainty Fitting algorithm, version 2 (SUFI-2), in SWAT-CUP [38].

Monthly streamflow observations from the Shirgah hydrometric station were used for calibration and validation. The model was calibrated for 2006–2014 and validated for 2015–2020 without further parameter adjustment.

Both calibration and validation used the 2001 LU/LC map, which provides the historical baseline for comparison with the later historical and projected maps. A sensitivity analysis first identified the parameters that most strongly influence monthly streamflow. These parameters were then adjusted within physically acceptable ranges over 11 iterations of 2,000 simulations each to improve the agreement between observed and simulated discharge. Supplementary Table S1 lists the retained parameters and how each was adjusted. The calibrated parameter set was retained during validation and applied to the 2012, 2023, 2034, and 2045 maps without map-specific recalibration.

Model performance was evaluated with the Nash–Sutcliffe efficiency (NSE), the coefficient of determination (R^2), and percent bias (PBIAS), which describe the agreement between observed and simulated streamflow, their linear association, and systematic bias, respectively [39–41]. Following Moriasi et al. [41], monthly streamflow simulation at the watershed scale was considered satisfactory when NSE > 0.50, R^2 > 0.60, and PBIAS was within ±15%.

LU/LC map simulations

After calibration and validation, the calibrated SWAT model was run with each of the five LU/LC maps (2001, 2012, 2023, 2034, and 2045). Between runs, only the LU/LC map changed; climate inputs, calibrated parameters, soil data, DEM, and HRU thresholds were kept constant. This fixed-climate design isolates the effect of land cover change from climate variability [2]. Crop management was treated as an integral part of agricultural land use: the same crop proportions, planting, harvesting, and irrigation dates, and irrigation amounts per crop were applied to agricultural HRUs in every simulation, so that the expansion or contraction of agricultural land carried its management, including irrigation, with it. The simulated responses therefore represent the combined effect of LU/LC change and the management associated with agricultural land.

Simulations were compared over the common period 2006–2020; the years in the map labels identify the LU/LC maps, not the years of climatic forcing. Hydrological responses were evaluated as watershed-averaged water-balance components and as streamflow at the Shirgah outlet (FLOW_OUT). The components were surface runoff (SURQ), water yield (WYLD), actual evapotranspiration (ET), percolation (PERC), groundwater contribution (GW_Q), and lateral flow (LATQ). For each LU/LC map, mean values over 2006–2020 and changes relative to the 2001 baseline were calculated. Values are reported rounded (areas and water-balance components to one decimal place, discharge to two); differences and percentage changes were calculated from unrounded values and may therefore differ slightly from differences between the rounded values. Annual outlet discharge was calculated from the monthly FLOW_OUT series at the outlet reach by weighting each monthly mean by the number of days in the month, including leap years. The mean for each map is the arithmetic mean of the 15 annual values

for 2006–2020, the same years used for the water balance, and the standard deviation across these years describes interannual variability, not parameter uncertainty. To compare outlet flow with water yield, annual discharge was also converted to a depth using the modelled basin area of each map and the actual number of days per year. To identify the cover groups contributing to differences between maps, HRUs were grouped by land-cover code. The basin-equivalent SURQ contribution of a group was calculated by multiplying the runoff depth of every HRU by its area, summing within the group and dividing by the total modelled basin area; the area-weighted SURQ was obtained by dividing this sum by the group area.

Results and discussion

LU/LC classification accuracy

The historical LU/LC maps for 2001, 2012 and 2023 were evaluated using independent validation polygons that were not used for training. Overall accuracy was 93.0% for 2001 (support vector machine, SVM), 91.9% for 2012 and 91.4% for 2023 (maximum likelihood classifier, MLC), with Kappa coefficients of 0.810, 0.788 and 0.780, respectively (Table 1). The confusion matrices are given in Supplementary Tables S2–S4.

Table 1. Overall accuracy of the historical LU/LC maps.

Year	Classifier	Overall accuracy (%)	Kappa
2001	Support vector machine (SVM)	93.0	0.810
2012	Maximum likelihood classification (MLC)	91.9	0.788
2023	Maximum likelihood classification (MLC)	91.4	0.780

Accuracy was calculated in ENVI 5.3 for agriculture, barren land, rangeland and forest. Residential areas (0.3–0.5% of the watershed; 533.2–864.7 ha) were added in a separate step and were not included in the accuracy assessment.

Forest was mapped most accurately in all years (producer's accuracy, PA, 95.7–98.6%; user's accuracy, UA, 98.5–99.6%), followed by rangeland (PA 77.3–83.1%, UA 73.8–82.0%; Supplementary Table S5). Barren land had the lowest PA (52.4–65.0%), which is attributable to confusion with rangeland, and agriculture had the lowest UA in 2012 and 2023 (50.1% and 54.2%), attributable to the misclassification of some forest and rangeland pixels as agriculture. Class-specific producer's and user's accuracies complement overall accuracy by describing omission and commission errors for individual land-cover classes [42].

To ensure complete independence from the training points, the validation polygons were digitised at non-overlapping locations. Errors in historical LU/LC maps can affect estimates of land-cover transitions [43]. Land-cover misclassification can also introduce uncertainty into hydrological simulations [44], including SWAT-simulated water yield [45].

Validation of the LU/LC projection

The land-change simulation was validated against the classified 2023 map using a minimum bounding rectangle (MBR) of 1 × 1 without stratification. The $K_{standard}$, K_{no}, $K_{location}$ and $K_{locationStrata}$ values were 0.831, 0.882, 0.869 and 0.869, respectively. Quantity disagreement was 0.025 and allocation disagreement was 0.073. Quantity disagreement represents the mismatch caused by differences in the total aerial extent of each class, while allocation disagreement reflects discrepancies arising from the spatial displacement of classes despite agreement in net area [46].

Because quantity disagreement was substantially lower than allocation disagreement, the model reproduced the overall class totals with greater fidelity than their explicit spatial arrangement. Consequently, the projected maps should be interpreted as indicating the general trajectory of LU/LC change rather than the precise spatial configuration of individual changes. Furthermore, because the validation was conducted over an 11-year simulation period, caution is warranted when extrapolating these results to the 22-year projection horizon of 2045.

Spatiotemporal LU/LC changes

As illustrated in Figs. 3 and 4, between 2001 and 2045, forest declined by 17.6% (from 65,368.7 to 53,860.6 ha) and rangeland by 25.1% (from 85,654.2 to 64,121.8 ha). Conversely, agricultural land increased by 97.7% (from 13,876.2 to 27,439.5 ha), barren land expanded by 193.8% (from 9,797.2 to 28,787.9 ha), and residential areas grew by 61.8% (from 533.2 to 862.9 ha). Supplementary Table S6 provides a detailed breakdown of the class areas across all five maps.

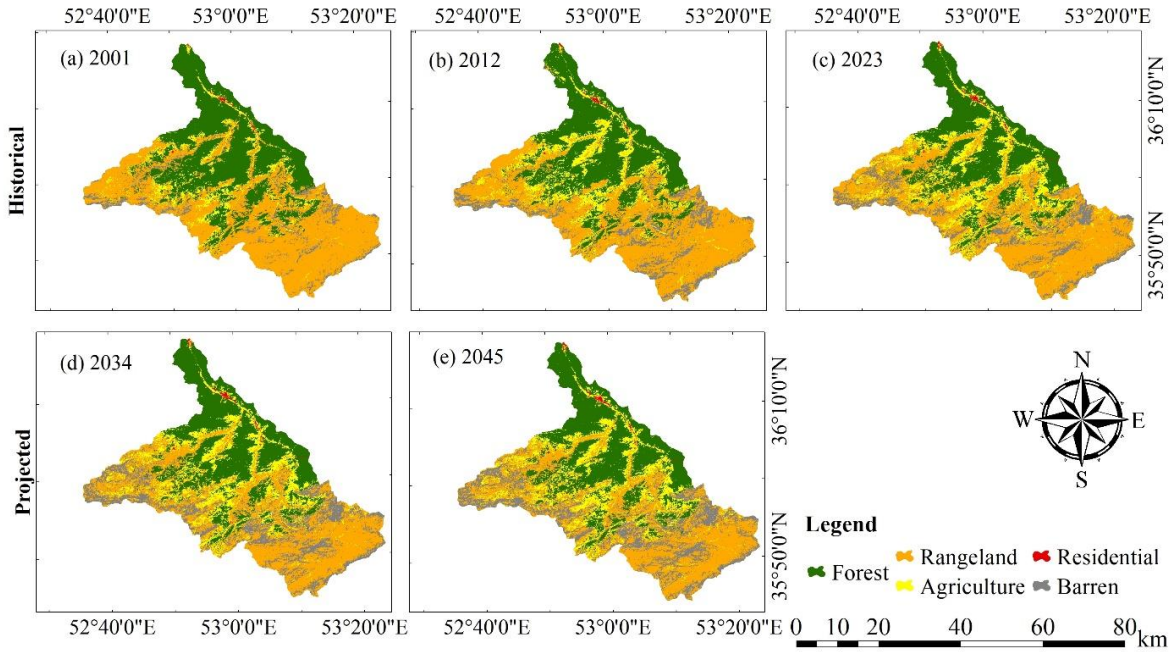


Fig. 3. Historical (2001, 2012 and 2023) and projected (2034 and 2045) LU/LC maps of the Talar Watershed, Iran.

Most of the agricultural expansion occurred before 2023, when the mapped agricultural area rose from 13,876.2 ha in 2001 to 27,360.9 ha in 2023, with minimal change thereafter (27,439.5 ha in 2045). Much of the historical change in all classes also occurred between 2001 and 2012 (agricultural land +8,702.8 ha, barren land +5,778.3 ha, forest −6,961.6 ha, and rangeland −7,834.1 ha), coinciding with the map transition that produced the largest increase in simulated surface runoff. While these combined land-cover transitions likely contributed to the hydrological response, this analysis does not attribute the simulated increase to any single class. From 2023 to 2045, the projected changes were dominated by rangeland loss (from 75,575.4 to 64,121.8 ha) and barren land expansion (from 17,070.9 to 28,787.9 ha). The projected maps thus describe declining vegetated cover and growing barren surfaces rather than continued agricultural expansion. Accordingly, these projections are employed as exploratory scenarios to examine potential hydrological consequences and should be considered indicative rather than definitive predictions of future change.

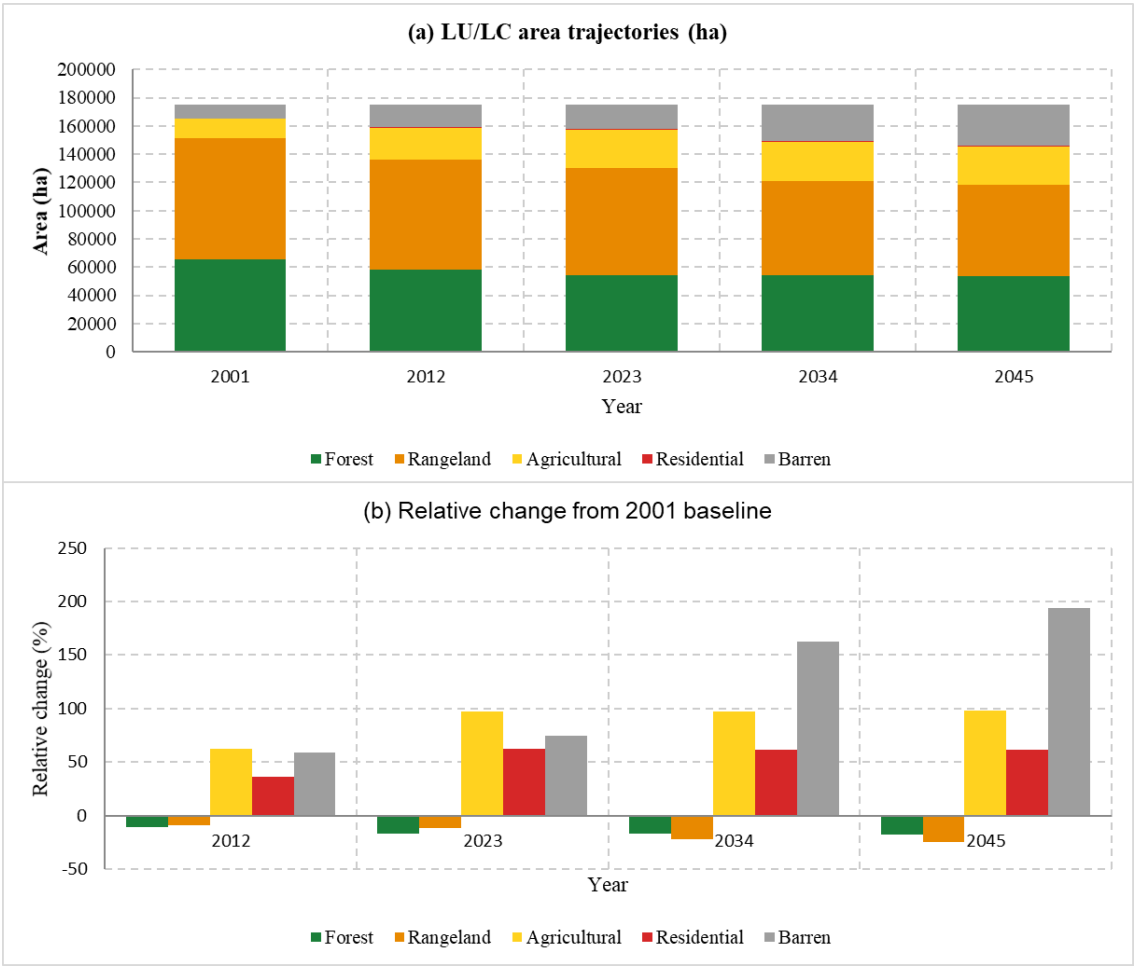


Fig. 4. Historical and projected LU/LC changes in the Talar Watershed: (a) area of each LU/LC class in 2001, 2012, 2023, 2034 and 2045; (b) relative change in each year compared with the 2001 baseline.

SWAT model performance

The most sensitive parameters were CN2 and the groundwater parameters GW_DELAY, ALPHA_BF, GWQMN and GW_REVAP, which control surface runoff generation and subsurface flow [37]. The final calibrated values are given in Supplementary Table S1.

The Nash–Sutcliffe efficiency (NSE) was 0.59 for calibration and 0.53 for validation, and the coefficient of determination (R^2) was 0.64 and 0.65, respectively (Table 2). PBIAS was 13.6% and 10.0%, indicating an underestimation of streamflow in both periods. Importantly, the findings from both periods met the established criteria for satisfactory monthly streamflow simulation at the watershed scale [41]. The P-factor values of 0.83 and 0.82 show that the 95% prediction uncertainty band (95PPU) enclosed 83% and 82% of the observed monthly values in the calibration and validation periods, and the corresponding R-factor values were 0.70 and 0.60. These indices describe the coverage and relative width of the uncertainty band [38].

Table 2. Performance of the SWAT monthly streamflow simulation at the Shirgah hydrometric station. NSE, Nash–Sutcliffe efficiency; R^2, coefficient of determination; PBIAS, percent bias; P-factor, proportion of observations

enclosed by the 95PPU band; R-factor, average width of the band divided by the standard deviation of the observed streamflow.

Period	Years	NSE	R^2	PBIAS (%)	P-factor	R-factor
Calibration	2006–2014	0.59	0.64	13.6	0.83	0.70
Validation	2015–2020	0.53	0.65	10.0	0.82	0.60

Despite some discrepancies in peak flows, the simulated hydrograph reproduced the general seasonal pattern of observed monthly streamflow (Fig. 5), consistent with the satisfactory performance statistics (Table 2). These deviations may reflect the sparse meteorological network, in which only four precipitation stations represent a steep elevation gradient of 203–3,857 m [47], uncertainties in snow accumulation and melt [48], and the spatial heterogeneity of soils and land cover [35]. As the individual contributions of these factors were not quantified, their relative importance remains uncertain.

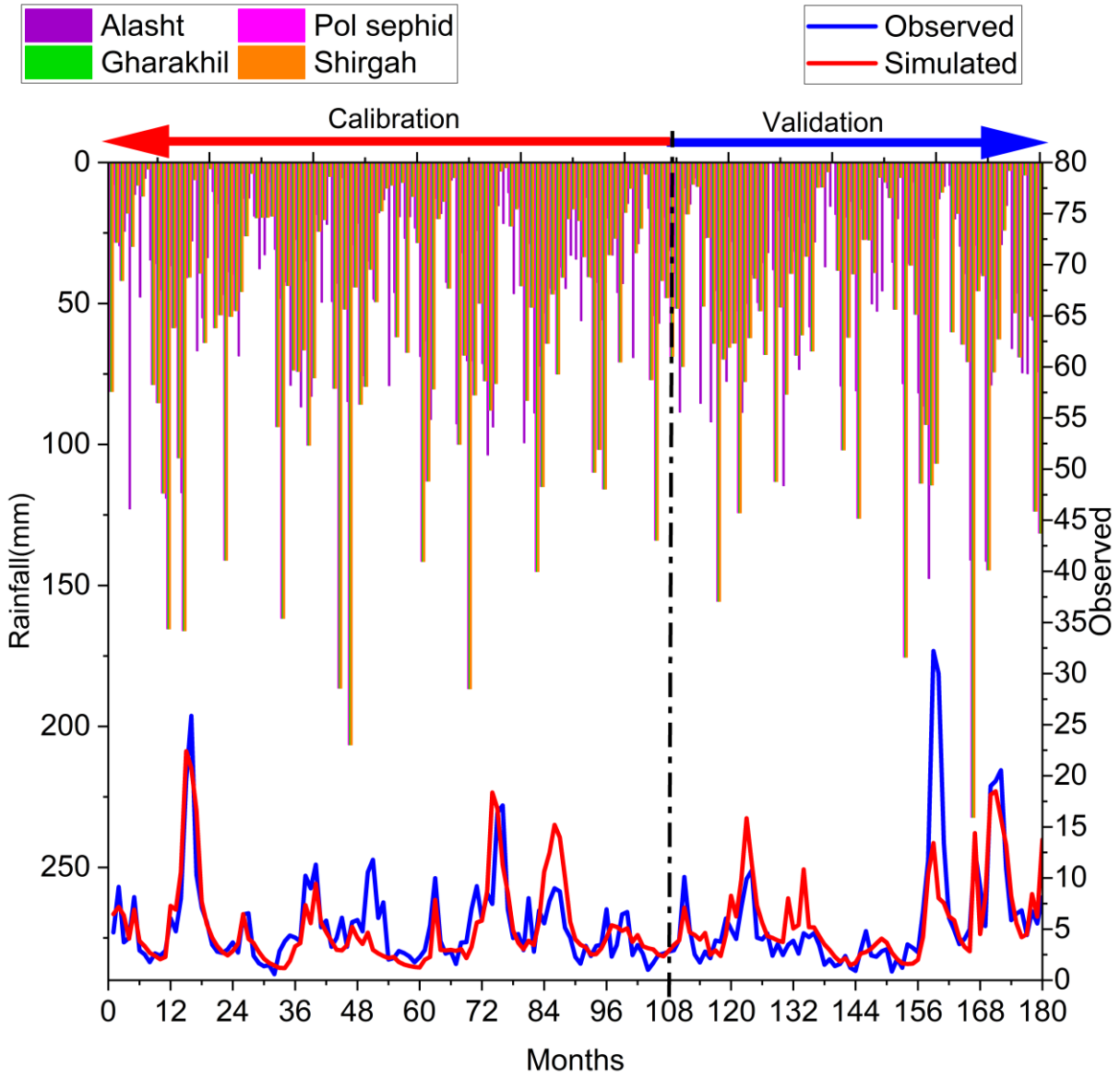


Fig. 5. Observed and simulated monthly streamflow at Shirgah during the calibration (2006–2014) and validation (2015–2020) periods, together with rainfall records from the Alasht, Pol Sefid, Gharakheil and Shirgah stations. The rainfall series represent individual station records, shown to illustrate local precipitation regimes rather than the watershed-average precipitation.

While calibration and validation focused exclusively on monthly streamflow at the watershed outlet, the remaining simulated water-balance components were not constrained by independent in situ observations, and streamflow-only calibration can allow different parameter sets to reproduce similar outlet discharge while yielding different internal fluxes (equifinality) [49,50]. Consequently, they should be viewed as comparative, model-based estimates of the hydrological response to each LU/LC configuration rather than as absolute values.

Water balance under the LU/LC maps

Table 3 shows the area-weighted mean annual water-balance components simulated for the five LU/LC maps over 2006–2020. Because all simulations shared identical climate series and the same simulation period, mean annual precipitation (587.5 mm in all maps) and potential evapotranspiration (PET; 1,075.4–1,076.3 mm) were nearly invariant across the maps; the small differences in PET reflect HRU area weighting. Relative to the 2001 baseline, all subsequent maps produced lower actual evapotranspiration (ET), percolation (PERC), groundwater contribution to streamflow (GW_Q) and lateral flow (LATQ), accompanied by higher surface runoff (SURQ) and water yield (WYLD).

Table 3. Area-weighted mean annual water-balance components simulated by SWAT for the five LU/LC maps, 2006–2020 (mm year^{-1}). PRECIP, precipitation; PET, potential evapotranspiration; ET, actual evapotranspiration; PERC, percolation below the soil profile; SURQ, surface runoff; GW_Q, shallow-aquifer contribution to streamflow; WYLD, water yield; LATQ, lateral flow. Values are means of 15 annual basin estimates, each weighted by HRU area. Differences and percentage changes in the text and in Fig. 6 were calculated from unrounded values.

LU/LC map	PRECIP	PET	ET	PERC	SURQ	GW_Q	WYLD	LATQ
2001	587.5	1,075.4	432.2	142.7	8.5	38.9	100.1	45.8
2012	587.5	1,076.3	393.6	98.3	54.1	28.4	127.7	40.4
2023	587.5	1,076.3	396.9	104.2	44.7	29.8	120.1	40.6
2034	587.5	1,076.3	393.7	98.2	54.8	28.3	127.7	39.9
2045	587.5	1,076.3	392.4	96.7	57.9	28.1	130.2	39.5

ET decreased from 432.2 mm in the baseline to 392.4–396.9 mm in the subsequent maps (8.2–9.2%), and PERC decreased from 142.7 to 96.7–104.2 mm (27.0–32.2%; Fig. 6a). Thus, less water returned to the atmosphere and less water moved below the soil profile. Because PERC is an internal transfer below the soil profile, it should not be added to ET and WYLD as an independent basin outflow when assessing water-balance closure [37].

SURQ increased from 8.5 mm in 2001 to 54.1, 44.7, 54.8 and 57.9 mm in the 2012, 2023, 2034 and 2045 maps, respectively. These values correspond to increases of 536.7%, 426.5%, 544.9% and 581.5% (36.2–49.4 mm year^{-1} in absolute terms; Fig. 6b), with the high percentage values largely reflecting the low baseline magnitude. SURQ was highest in 2045 and, among the subsequent maps, lowest in 2023; the response therefore did not increase steadily with map year.

GW_Q decreased from 38.9 to 28.1–29.8 mm and LATQ from 45.8 to 39.5–40.6 mm. Nevertheless, WYLD increased from 100.1 mm to 127.7, 120.1, 127.7 and 130.2 mm in the four subsequent maps. Because the increase in SURQ exceeded the combined reduction in GW_Q and LATQ, surface runoff made up a larger proportion of water yield than in 2001 (from

8.5% to 37.2–44.5%). The higher water yield was thus characterised by a shift toward surface flow at the expense of subsurface contributions.

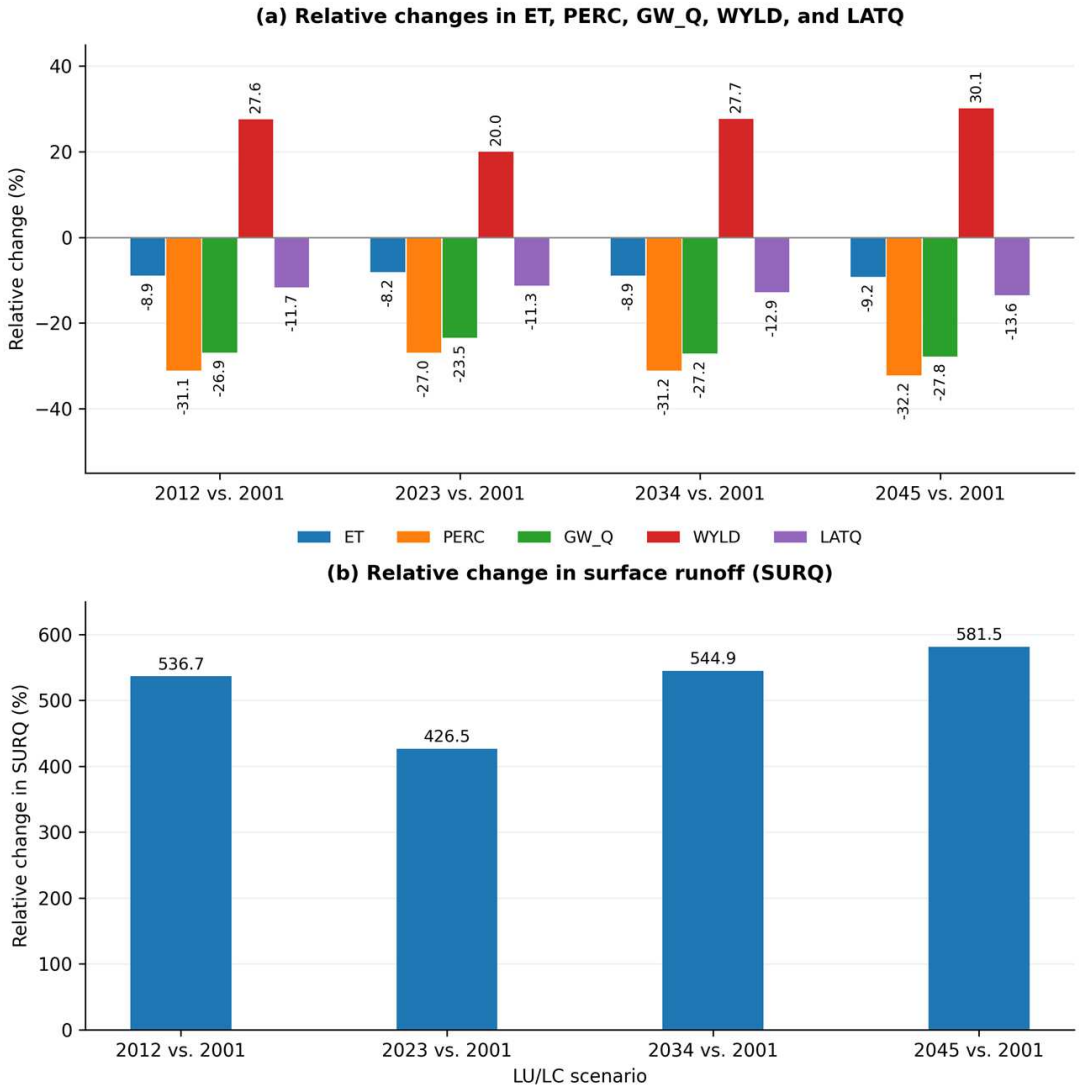


Fig. 6. Relative changes in SWAT-simulated mean annual water-balance components under the 2012, 2023, 2034 and 2045 LU/LC maps compared with the 2001 baseline (2006–2020): (a) ET, PERC, GW_Q, WYLD and LATQ; (b) SURQ. Percentages were calculated from unrounded area-weighted basin means.

The 2023 map responded in the same direction as the projected scenarios but with reduced magnitude. Relative to 2012, SURQ was 9.4 mm lower (−17.3%) and WYLD was 7.5 mm lower (−5.9%), whereas ET, PERC, GW_Q and LATQ were higher by 3.3, 5.9, 1.3 and 0.2 mm, respectively. Grouping the HRUs by land-cover code showed that the basin-equivalent SURQ contribution of barren-land HRUs decreased from 24.9 to 18.6 mm and that of rangeland HRUs from 18.1 to 12.5 mm (combined decrease 11.8 mm), which was partly offset by increases in other groups. Furthermore, the area-weighted SURQ within barren-land HRUs declined from 274.4 to 207.8 mm and within rangeland HRUs from 40.6 to 29.9 mm; thus, the reduction did not stem solely from changes in group area.

In contrast, the combined contribution of the six agricultural groups increased from 6.6 to 8.5 mm as their represented area expanded from 23,087.9 to 30,356.9 ha. This was accompanied by only minor variations in crop proportions, which stemmed from the fixed crop fractions assigned to agricultural land and the HRU delineation process rather than mapped crop distributions (rice 33.5% to 35.0%, apple 10.0% to 11.0%, and winter wheat 16.6% to 15.0%; Supplementary Table S7). Accordingly, the lower basin runoff in 2023 cannot be attributed to the agricultural HRUs.

Outlet streamflow response

As illustrated in Fig. 7, mean annual streamflow at the Shirgah outlet increased from 5.40 $m^3 s^{-1}$ in the 2001 baseline to 6.79, 6.36, 6.79 and 6.93 $m^3 s^{-1}$ under the 2012, 2023, 2034 and 2045 maps, respectively. These changes represent increases of 1.39, 0.96, 1.39 and 1.52 $m^3 s^{-1}$ (25.7%, 17.7%, 25.6% and 28.2%). Among the subsequent maps, the discharge response peaked in 2045 and was lowest in 2023, whereas the 2012 and 2034 means differed by less than 0.01 m^3 s−1.

Fig. 7. Mean annual streamflow at the Shirgah outlet under the five LU/LC maps in 2006–2020. Bars represent the means of 15 annual discharge values; error bars show ±1 sample standard deviation across years (n = 15 per map). Annual discharge was calculated from monthly FLOW_OUT with month-length weighting. The dashed line marks the 2001 baseline mean.

The interannual standard deviation was 2.47 $m^3 s^{-1}$ in the baseline and ranged from 2.67 to 2.79 $m^3 s^{-1}$ across the subsequent maps. Supplementary Table S8 provides additional detail on the year-by-year comparisons. Annual discharge exceeded the baseline in 13 of 15 years for the 2012, 2034 and 2045 maps and in 12 of 15 years for 2023. All four subsequent maps yielded lower discharge than the baseline in 2007 and 2013, with the 2023 map also exhibiting a slight reduction in 2010. Consequently, the simulated increase applies to the long-term mean rather than to every year.

The outlet response mirrored the pattern of water yield: the 2045 map had the largest WYLD and outlet discharge, and 2023 had smaller increases in both than 2012. Relative to 2012, the 2023 map reduced the mean outlet discharge by 0.43 $m^3 s^{-1}$ (6.4%), in line with the 7.5 mm reduction in WYLD described above.

The percentage changes in SURQ (426.5–581.5%) were substantially larger than those in outlet discharge (17.7–28.2%). This divergence is partly attributable to the low baseline value of SURQ and the concurrent decline in groundwater and lateral-flow contributions. In addition, outlet discharge is a routed channel output, whereas WYLD is the water delivered from the landscape to the channel network [37]; hence, the two metrics are not necessarily identical even when converted to equivalent area-depth units. The mean outlet-flow depths were 97.4, 122.4, 114.6, 122.3 and 124.8 mm $year^{-1}$, compared with WYLD values of 100.1, 127.7, 120.1, 127.7 and 130.2 mm $year^{-1}$ (Supplementary Table S9). These minor discrepancies (2.7–5.5 mm $year^{-1}$) are presented as a diagnostic comparison and should not be attributed entirely to channel transmission losses.

Discussion

The simulations show that replacing the 2001 land cover with the later historical and projected maps shifted the simulated water balance from subsurface pathways toward surface runoff. Relative to the 2001 baseline, actual evapotranspiration and percolation decreased by 8.2–9.2% and 27.0–32.2%, while groundwater contribution and lateral flow declined by 23.5–27.8% and 11.3–13.6%, respectively. Conversely, surface runoff increased from 8.5 to 44.7–57.9 mm year−1, accompanied by an elevation

in mean outlet discharge of 17.7–28.2%. The historical maps were classified with overall accuracies of 91.4–93.0%, and the calibrated model reproduced monthly streamflow satisfactorily (NSE 0.53–0.59), thereby supporting this controlled, scenario-based comparison. Nevertheless, because the 2034 and 2045 maps represent exploratory projections rather than definitive forecasts, caution is warranted when interpreting these future hydrological responses.

The direction of these simulated changes aligns broadly with previous modelling investigations. In the Palico watershed, forest and rangeland loss increased simulated surface runoff and reduced baseflow and groundwater recharge [51]. Similarly, within the Talar River basin, Kavian et al. [12] reported an increase in streamflow driven by forest conversion and agricultural expansion. Although their reported increase of 34.4% for the 1991–2013 period exceeds the 17.7–28.2% range obtained in the present study, differences in basin extent, simulation period and map construction prevent a direct comparison of effect sizes.

Comparable land-cover change has also been linked to greater simulated surface runoff and water yield in the Akaki catchment [52] and to higher surface runoff with lower lateral flow and percolation in the İznik Lake Watershed [53], although the response differs among periods and spatial scales [54]. The lower ET is consistent with SWAT results for the Samin catchment, Indonesia, where forest loss and the expansion of agricultural and settlement land reduced the ratio of evapotranspiration to rainfall from 60% to 54.8%, although that change was not statistically significant at the 5% level [55]. Using the WaSiM model, Sulamo et al. likewise simulated an ET decrease of about 6% between 1989 and 2015 in the Bilate watershed, Ethiopia [56], and a remote-sensing study in the Narmada basin, India, projected lower ET with continued forest removal [57]. While studies integrating simultaneous LU/LC shifts with climate variability [58] provide valuable context, they are not directly comparable to the decoupled, fixed-climate framework implemented here. The land-cover trends themselves are consistent with the pressures from agriculture, construction, grazing and mining described for the Talar Watershed [12,13].

In SWAT, water partitioning depends on the combination of land cover, soil, slope, and management within each HRU [37]; consequently, the average response of a land-cover group can change even when its mapped area changes in the opposite direction. The smaller response of the 2023 map relative to 2012 (SURQ 9.4 mm lower) was associated with reduced contributions from barren-land and rangeland HRUs and cannot be accounted for by the agricultural HRUs. Together with the nearly equal outlet-flow means for 2012 and 2034, these patterns demonstrate that the simulated hydrological response did not increase uniformly with the year of the LU/LC map. Attributing the response to specific soil–slope combinations or land-cover conversions would require matching the HRU characteristics across maps.

The principal management implication is that greater annual flow does not necessarily indicate improved water availability throughout the year, because the higher water yield was accompanied by smaller subsurface contributions. Assessing land-use outcomes in the Talar Watershed therefore requires attention to the partitioning of water between surface and subsurface pathways, as well as total annual discharge. The findings provide a basin-scale basis for considering hydrological consequences in land-use assessment. They do not establish changes in dry-season flow reliability or flood frequency, identify priority subbasins, demonstrate the effectiveness of restoration measures, or establish the feasibility of a payment-for-ecosystem-services programme; such decisions require spatial and intervention-specific evidence beyond the comparisons undertaken here.

Despite these contributions, several limitations of the present study must be acknowledged. First, each static LU/LC map was evaluated over the same 2006–2020 climate sequence, so the design supports a controlled comparison but does not reconstruct historical year-by-year land-use change, and the 2034 and 2045 maps are exploratory projections based on past transitions that exclude future climate change and alternative policy pathways. Second, classification accuracy and the agreement between simulated

and reference 2023 maps do not quantify uncertainty in the hydrological response; classification and allocation errors were not propagated through alternative maps, although categorical uncertainty in LU/LC inputs can affect SWAT-simulated water yield [45].

Third, calibration and validation were constrained to monthly outlet discharge alone. ET, PERC, GW_Q and LATQ were not independently validated, flood peaks and dry-season flows were not evaluated, and the results come from one calibrated parameter set, so the annual standard deviations describe interannual variability rather than parameter uncertainty and the magnitude of the differences among maps remains conditional on the parameterisation [35]. Fourth, the HRU composition changes with the LU/LC input and the represented class areas may differ from the original map areas after thresholding [59], so the group-level comparison identifies contributions to the simulated response but does not separate the effects of land-cover transitions, soil–slope combinations, HRU redistribution and routing.

Fifth, crop proportions and management schedules were fixed assumptions rather than mapped crop data, irrigation amounts were estimated rather than measured, and no map-specific irrigation and reach water budget was available, so irrigation, channel losses and storage changes cannot be fully separated from the overall simulated response. Finally, soil erosion, ecological feedbacks, stakeholder priorities and intervention costs were not evaluated, so the implications are restricted to the simulated hydrological responses.

Future investigations are needed to establish whether the contrasts among maps persist across acceptable parameter sets and alternative LU/LC realisations, using independent observations to constrain internal water fluxes, and to evaluate seasonal flow with explicit accounting of irrigation and channel water transfers. Such evaluations would clarify whether the annual increases translate into changes relevant to water-supply reliability and high-flow management.

Conclusions

This study used SWAT to compare the hydrological responses of the Talar Watershed to historical and projected LU/LC maps under a common 2006–2020 climate series. The comparison evaluates alternative land-cover maps; the 2034 and 2045 simulations represent exploratory LU/LC projections rather than forecasts of future streamflow.

Relative to the 2001 baseline, all later maps produced greater surface runoff and water yield, together with lower actual evapotranspiration, percolation, groundwater contribution and lateral flow. Mean outlet discharge increased from 5.40 $m^3 s^{-1}$ to 6.79, 6.36, 6.79 and 6.93 $m^3 s^{-1}$ under the 2012, 2023, 2034 and 2045 maps, respectively, corresponding to increases of 17.7–28.2%. The strongest mean outlet response occurred under the 2045 map.

The smaller response under the 2023 map indicates that simulated hydrological change did not increase uniformly with the year of the LU/LC map. HRU-level comparisons associated its lower surface runoff relative to 2012 with reduced contributions from barren land and rangeland, partly offset by increases from other cover groups. These comparisons identify the contributions to the simulated difference, but do not establish the independent effects of individual land conversions or their locations.

The main implication is that increased annual discharge can coexist with reduced subsurface contributions and therefore does not, by itself, establish improved water availability during dry periods. These findings support basin-scale assessment of water partitioning under LU/LC change. Accordingly, their interpretation remains conditional on the mapped land cover and calibrated model configuration, with validation restricted to monthly outlet discharge. Seasonal-flow evaluation and propagation of map and parameter uncertainty would strengthen their use in water-resource assessment.

Data availability

The Landsat Collection 2 Level-2 surface reflectance imagery (August 2001, May 2012 and August 2023) and the 30 m SRTM digital elevation model are publicly available from the USGS EarthExplorer (https://earthexplorer.usgs.gov/) and Google Earth Engine (https://earthengine.google.com/). The soil map and its attributes were taken from Mohammadi et al. Daily precipitation and temperature records were provided by the Iran Meteorological Organization (IRIMO), and daily precipitation and streamflow records for the Shirgah hydrometric station were obtained from the Ministry of Energy of Iran; these records can be requested from the respective organizations. The calibrated SWAT parameters, the confusion matrices and class-wise accuracies, the LU/LC class areas, the agricultural composition of the HRUs, and the annual discharge and water-yield comparisons are provided in the Supplementary Information. The classified LU/LC maps (2001, 2012 and 2023), the projected maps (2034 and 2045) and the SWAT outputs generated and analysed in this study are available from the corresponding author (H.M.) on reasonable request.

References

1. Saddique, N., Mahmood, T. & Bernhofer, C. Quantifying the impacts of land use/land cover change on the water balance in the afforested River Basin, Pakistan. *Environ. Earth Sci.* **79,** 448 (2020). https://doi.org/10.1007/s12665-020-09206-w
2. Khorn, N., Ismail, M. H., Nurhidayu, S., Kamarudin, N. & Sulaiman, M. S. Land use/land cover changes and its impact on runoff using SWAT model in the Upper Prek Thnot watershed in Cambodia. *Environ. Earth Sci.* **81,** 466 (2022). https://doi.org/10.1007/s12665-022-10583-7
3. Negash, T. W., Abagale, F. K. & Baatuuwie, B. N. Impact of land-use and land-cover change on watershed hydrology: a case study of Mojo watershed, Ethiopia. *Environ. Earth Sci.* **81,** 536 (2022). https://doi.org/10.1007/s12665-022-10660-x
4. Banjara, M., Bhusal, A., Ghimire, A. B. & Kalra, A. Impact of land use and land cover change on hydrological processes in urban watersheds: analysis and forecasting for flood risk management. *Geosciences* **14,** 40 (2024). https://doi.org/10.3390/geosciences14020040
5. Sun, Y. & Zhang, J. Advances in research on the impact of land use/cover changes on watershed hydrological processes. *Front. Sustain. Dev.* **5,** 193–196 (2025). https://doi.org/10.54691/5xyggb72
6. Mas, J.-F., Kolb, M., Paegelow, M., Camacho Olmedo, M. T. & Houet, T. Inductive pattern-based land use/cover change models: a comparison of four software packages. *Environ. Model. Softw.* **51,** 94–111 (2014). https://doi.org/10.1016/j.envsoft.2013.09.010
7. Eastman, J. R. *TerrSet 2020 Geospatial Monitoring and Modeling System Manual* (Clark Labs, Clark University, 2020). https://www.clarku.edu/geospatial-analytics/terrset/download/
8. Beroho, M. et al. Future scenarios of land use/land cover (LULC) based on a CA-Markov simulation model: case of a Mediterranean watershed in Morocco. *Remote Sens.* **15,** 1162 (2023). https://doi.org/10.3390/rs15041162
9. Mekonnen, Y. A. & Manderso, T. M. Land use/land cover change impact on streamflow using Arc-SWAT model, in case of Fetam watershed, Abbay Basin, Ethiopia. *Appl. Water Sci.* **13,** 111 (2023). https://doi.org/10.1007/s13201-023-01914-5
10. Ware, H. H., Chang, S. W., Lee, J. E. & Chung, I.-M. Assessment of hydrological responses to land use and land cover changes in forest-dominated watershed using SWAT model. *Water* **16,** 528 (2024). https://doi.org/10.3390/w16040528
11. UNESCO World Heritage Centre. Hyrcanian Forests. https://whc.unesco.org/en/list/1584/ (2019).
12. Kavian, A., Mohammadi, M., Gholami, L. & Rodrigo-Comino, J. Assessment of the spatiotemporal effects of land use changes on runoff and nitrate loads in the Talar River. *Water* **10,** 445 (2018). https://doi.org/10.3390/w10040445
13. Zabihi, M., Moradi, H., Gholamalifard, M., Khaledi Darvishan, A. & Fürst, C. Landscape management through change processes monitoring in Iran. *Sustainability* **12,** 1753 (2020). https://doi.org/10.3390/su12051753

14. Mirakhorlo, M. S. & Rahimzadegan, M. Analysing the land-use change effects on soil erosion and sediment in the North of Iran; a case study: Talar watershed. *Geocarto Int.* **36,** 936–956 (2021). https://doi.org/10.1080/10106049.2019.1624985
15. Mohammadi, M. et al. Analysis of the impact of land use changes on soil erosion intensity and sediment yield using the IntErO model in the Talar Watershed of Iran. *Water* **13,** 881 (2021). https://doi.org/10.3390/w13060881
16. Mirchooli, F., Mohammadi, M. & Sadeghi, S. H. Spatial modeling of relationship between soil erosion factors and land-use changes at sub-watershed scale for the Talar watershed, Iran. *Nat. Hazards* **116,** 3703–3723 (2023). https://doi.org/10.1007/s11069-023-05832-2
17. Ruigar, H., Emamgholizadeh, S., Gharechelou, S. & Golian, S. Evaluating the impacts of anthropogenic, climate, and land use changes on streamflow. *J. Water Clim. Change* **15,** 1885–1905 (2024). https://doi.org/10.2166/wcc.2024.664
18. Nkwasa, A., Chawanda, C. J., Jägermeyr, J. & van Griensven, A. Improved representation of agricultural land use and crop management for large-scale hydrological impact simulation in Africa using SWAT+. *Hydrol. Earth Syst. Sci.* **26,** 71–89 (2022). https://doi.org/10.5194/hess-26-71-2022
19. Wei, X. et al. Hydrologic analysis of an intensively irrigated area in Southern Peru using a crop-field scale framework. *Water* **13,** 318 (2021). https://doi.org/10.3390/w13030318
20. Marek, G. W. et al. Modeling long-term water use of irrigated cropping rotations in the Texas High Plains using SWAT. *Irrig. Sci.* **35,** 111–123 (2017). https://doi.org/10.1007/s00271-016-0524-6
21. Earth Resources Observation and Science (EROS) Center. Landsat 7 Enhanced Thematic Mapper Plus Level-2, Collection 2. U.S. Geological Survey https://doi.org/10.5066/P9C7I13B (2020).
22. Earth Resources Observation and Science (EROS) Center. Landsat 4–5 Thematic Mapper Level-2, Collection 2. U.S. Geological Survey https://doi.org/10.5066/P9IAXOVV (2020).
23. Earth Resources Observation and Science (EROS) Center. Landsat 8–9 Operational Land Imager/Thermal Infrared Sensor Level-2, Collection 2. U.S. Geological Survey https://doi.org/10.5066/P9OGBGM6 (2020).
24. Gorelick, N. et al. Google Earth Engine: planetary-scale geospatial analysis for everyone. *Remote Sens. Environ.* **202,** 18–27 (2017). https://doi.org/10.1016/j.rse.2017.06.031
25. Masek, J. G. et al. A Landsat surface reflectance dataset for North America, 1990–2000. *IEEE Geosci. Remote Sens. Lett.* **3,** 68–72 (2006). https://doi.org/10.1109/LGRS.2005.857030
26. Vermote, E., Justice, C., Claverie, M. & Franch, B. Preliminary analysis of the performance of the Landsat 8/OLI land surface reflectance product. *Remote Sens. Environ.* **185,** 46–56 (2016). https://doi.org/10.1016/j.rse.2016.04.008
27. Farr, T. G. et al. The Shuttle Radar Topography Mission. *Rev. Geophys.* **45,** RG2004 (2007). https://doi.org/10.1029/2005RG000183
28. Mohammadi, M., Kavian, A. & Gholami, L. Simulation of discharge and nitrate in Tallar Basin using SWAT model (in Persian). *J. Watershed Manag. Res.* **8,** 45–60 (2017). https://doi.org/10.29252/jwmr.8.15.45
29. Soil and Water Research Institute. http://www.swri.ir/
30. Zha, Y., Gao, J. & Ni, S. Use of normalized difference built-up index in automatically mapping urban areas from TM imagery. *Int. J. Remote Sens.* **24,** 583–594 (2003). https://doi.org/10.1080/01431160304987
31. Rouse, J. W., Haas, R. H., Schell, J. A. & Deering, D. W. Monitoring vegetation systems in the Great Plains with ERTS. In Third Earth Resources Technology Satellite-1 Symposium Vol. 1, Section A, 309–317 (NASA SP-351, 1974). https://ntrs.nasa.gov/citations/19740022614
32. Xu, H. Modification of normalised difference water index (NDWI) to enhance open water features in remotely sensed imagery. *Int. J. Remote Sens.* **27,** 3025–3033 (2006). https://doi.org/10.1080/01431160600589179
33. Ghayour, L. et al. Performance evaluation of Sentinel-2 and Landsat 8 OLI data for land cover/use classification using a comparison between machine learning algorithms. *Remote Sens.* **13,** 1349 (2021). https://doi.org/10.3390/rs13071349
34. Pontius, R. G., Jr. Quantification error versus location error in comparison of categorical maps. *Photogramm. Eng. Remote Sens.* **66,** 1011–1016 (2000). https://www.asprs.org/wp-content/uploads/pers/2000journal/august/2000_aug_1011-1016.pdf
35. Arnold, J. G. et al. SWAT: Model use, calibration, and validation. *Trans. ASABE* **55,** 1491–1508 (2012). https://doi.org/10.13031/2013.42256

36. Arnold, J. G., Srinivasan, R., Muttiah, R. S. & Williams, J. R. Large area hydrologic modeling and assessment part I: model development. *J. Am. Water Resour. Assoc.* **34,** 73–89 (1998). https://doi.org/10.1111/j.1752-1688.1998.tb05961.x
37. Neitsch, S. L., Arnold, J. G., Kiniry, J. R. & Williams, J. R. *Soil and Water Assessment Tool Theoretical Documentation, Version 2009*. Technical Report No. 406 (Texas Water Resources Institute, 2011). https://hdl.handle.net/1969.1/128050
38. Abbaspour, K. C. *SWAT-CUP: SWAT Calibration and Uncertainty Programs—A User Manual* (Eawag, 2015). https://swat.tamu.edu/media/114860/usermanual_swatcup.pdf
39. Nash, J. E. & Sutcliffe, J. V. River flow forecasting through conceptual models part I—a discussion of principles. *J. Hydrol.* **10,** 282–290 (1970). https://doi.org/10.1016/0022-1694(70)90255-6
40. Gupta, H. V., Sorooshian, S. & Yapo, P. O. Status of automatic calibration for hydrologic models: comparison with multilevel expert calibration. *J. Hydrol. Eng.* **4,** 135–143 (1999). https://doi.org/10.1061/(ASCE)1084-0699(1999)4:2(135)
41. Moriasi, D. N., Gitau, M. W., Pai, N. & Daggupati, P. Hydrologic and water quality models: Performance measures and evaluation criteria. *Trans. ASABE* **58,** 1763–1785 (2015). https://doi.org/10.13031/trans.58.10715
42. Olofsson, P. et al. Good practices for estimating area and assessing accuracy of land change. *Remote Sens. Environ.* **148,** 42–57 (2014). https://doi.org/10.1016/j.rse.2014.02.015
43. Pontius, R. G., Jr. & Li, X. Land transition estimates from erroneous maps. *J. Land Use Sci.* **5,** 31–44 (2010). https://doi.org/10.1080/17474230903222473
44. Miller, S. N., Guertin, D. P. & Goodrich, D. C. Hydrologic modeling uncertainty resulting from land cover misclassification. *J. Am. Water Resour. Assoc.* **43,** 1065–1075 (2007). https://doi.org/10.1111/j.1752-1688.2007.00088.x
45. Pai, N. & Saraswat, D. Impact of land use and land cover categorical uncertainty on SWAT hydrologic modeling. *Trans. ASABE* **56,** 1387–1397 (2013). https://doi.org/10.13031/trans.56.10062
46. Pontius, R. G., Jr. & Millones, M. Death to Kappa: Birth of quantity disagreement and allocation disagreement for accuracy assessment. *Int. J. Remote Sens.* **32,** 4407–4429 (2011). https://doi.org/10.1080/01431161.2011.552923
47. Galván, L., Olías, M., Izquierdo, T., Cerón, J. C. & Fernández de Villarán, R. Rainfall estimation in SWAT: An alternative method to simulate orographic precipitation. *J. Hydrol.* **509,** 257–265 (2014). https://doi.org/10.1016/j.jhydrol.2013.11.044
48. Ahl, R. S., Woods, S. W. & Zuuring, H. R. Hydrologic calibration and validation of SWAT in a snow-dominated Rocky Mountain watershed, Montana, U.S.A. *J. Am. Water Resour. Assoc.* **44,** 1411–1430 (2008). https://doi.org/10.1111/j.1752-1688.2008.00233.x
49. Beven, K. & Freer, J. Equifinality, data assimilation, and uncertainty estimation in mechanistic modelling of complex environmental systems using the GLUE methodology. *J. Hydrol.* **249,** 11–29 (2001). https://doi.org/10.1016/S0022-1694(01)00421-8
50. Shah, S. et al. Evaluating the added value of multi-variable calibration of SWAT with remotely sensed evapotranspiration data for improving hydrological modeling. *J. Hydrol.* **603,** 127046 (2021). https://doi.org/10.1016/j.jhydrol.2021.127046
51. Briones, R. U., Ella, V. B. & Bantayan, N. C. Hydrologic impact evaluation of land use and land cover change in Palico Watershed, Batangas, Philippines using the SWAT model. *J. Environ. Sci. Manag.* **19,** 96–107 (2016). https://doi.org/10.47125/jesam/2016_1/10
52. Maru, H., Haileslassie, A., Zeleke, T. & Teferi, E. Analysis of the impacts of land use land cover change on streamflow and surface water availability in Awash Basin, Ethiopia. *Geomat. Nat. Hazards Risk* **14,** 1–25 (2023). https://doi.org/10.1080/19475705.2022.2163193
53. Tezel, A. Ç., Akpınar, A., Bor, A. & Alfredsen, K. T. Exploring hydrological response to land use/land cover change using the SWAT+ model in the İznik Lake Watershed, Türkiye. *Water* **17,** 1924 (2025). https://doi.org/10.3390/w17131924
54. Abuhay, W., Gashaw, T. & Tsegaye, L. Assessing impacts of land use/land cover changes on the hydrology of Upper Gilgel Abbay watershed using the SWAT model. *J. Agric. Food Res.* **12,** 100535 (2023). https://doi.org/10.1016/j.jafr.2023.100535
55. Marhaento, H., Booij, M. J., Rientjes, T. H. M. & Hoekstra, A. Y. Attribution of changes in the water balance of a tropical catchment to land use change using the SWAT model. *Hydrol. Process.* **31,** 2029–2040 (2017). https://doi.org/10.1002/hyp.11167

56. Sulamo, M. A., Kassa, A. K. & Roba, N. T. Evaluation of the impacts of land use/cover changes on water balance of Bilate watershed, Rift valley basin, Ethiopia. *Water Pract. Technol.* **16**, 1108–1127 (2021). https://doi.org/10.2166/wpt.2021.063
57. Kundu, S., Mondal, A., Khare, D., Hain, C. & Lakshmi, V. Projecting climate and land use change impacts on actual evapotranspiration for the Narmada River Basin in Central India in the future. *Remote Sens.* **10,** 578 (2018). https://doi.org/10.3390/rs10040578
58. Pandi, D., Kothandaraman, S. & Kuppusamy, M. Water balance dynamics under climate variability and LULC changes—a catchment scale assessment. *Appl. Water Sci.* **15,** 244 (2025). https://doi.org/10.1007/s13201-025-02600-4
59. Her, Y., Frankenberger, J., Chaubey, I. & Srinivasan, R. Threshold effects in HRU definition of the Soil and Water Assessment Tool. *Trans. ASABE* **58,** 367–378 (2015). https://doi.org/10.13031/trans.58.10805

Acknowledgements

During the preparation of this work, the authors used ChatGPT and Grammarly to shorten sentences and check grammar. After using these tools, the authors reviewed and edited the content as needed and take full responsibility for the content of the publication.

Author contributions

F.K.S. contributed to conceptualization, methodology, data curation and writing the original draft. H.M. contributed to conceptualization, supervision, funding acquisition, and reviewing and editing the manuscript. A.M., V.M. and P.D. contributed to conceptualization and to reviewing and editing the manuscript. All authors reviewed and approved the final manuscript.

Funding

This work is based on research funded by the Iran National Science Foundation (INSF) under project No. 4021694.

Declarations

Competing interests

The authors declare no competing interests.

Additional information

Correspondence and requests for materials should be addressed to H.M.

Supplementary Files

This is a list of supplementary files associated with this preprint. Click to download.

- SupplementaryInformation1.docx